



Hierarchical porous activated carbon derived from agro-waste for potential CO₂ capture and efficient dye removal applications

Amruta Koli¹ · Anil K. Battu² · Radha Kishan Motkuri³ · Sandip Sabale¹

Received: 5 May 2022 / Revised: 11 July 2022 / Accepted: 11 July 2022 / Published online: 20 July 2022
© The Author(s), under exclusive licence to Springer-Verlag GmbH Germany, part of Springer Nature 2022

Abstract

An approach to functionalize the chemical carbonization of a sugarcane pith is reported to utilize the readily available and abundant agro-waste that produces hierarchical porous activated carbon (AC) using a nitrogen activation strategy for CO₂ capture and environmental remediation. The obtained raw carbon (RC) and activated carbon (AC) were characterized for their structural, functional, elemental, morphological, and surface properties. The nitrogen-containing AC production with a surface area of 725 m²g⁻¹ and 0.3377 cm³ g⁻¹ pore volume is achieved. The nitrogen activation strategy for AC enhanced the CO₂ uptake capacity with high CO₂ selectivity over N₂. The isosteric heat of adsorption (Q_{st}), 28.79 kJmol⁻¹, suggests the strong physio-sorption interactions between CO₂ and hierarchical porous AC. Furthermore, the AC adsorbent was found efficient for the fast removal of methyl orange (MO) dye with an equilibrium capacity of ~ 527 mg g⁻¹. The obtained AC showed appreciable reusability for MO adsorption efficiency. Combining the selective CO₂ uptake with the high and fast dye removal capacity, this low-cost agro-waste-derived hierarchical porous AC has excellent potential for energy and environmental applications.

Keywords Hierarchical porous carbon · Sugarcane pith · Dye removal · CO₂ capture · Agro-waste

Highlights

- Chemical carbonization followed by physical activation methodology to produce hierarchical porous activated carbon (AC).
- AC from easily available agro-waste sugarcane pith (SCP) with high SSA (725 m² g⁻¹).
- Facilitates efficient CO₂ capture and fast removal of methyl orange dye.
- Isosteric heat of adsorption (28.79 kJmol⁻¹) suggests the strong physio-sorption.
- Low-cost agro-waste-derived hierarchical porous AC with potential for energy and environmental applications.

✉ Radha Kishan Motkuri
Radhakishan.Motkuri@pnnl.gov

✉ Sandip Sabale
srsabale@gmail.com

¹ Department of Chemistry, Jaysingpur College, Jaysingpur 416101, M.S., India

² Environmental Molecular Sciences Laboratory, Pacific Northwest National Laboratory, Richland, WA, USA

³ Energy and Environment Directorate, Pacific Northwest National Laboratory, Richland, WA, USA

1 Introduction

In the twentieth century, there was a rapid growth in industrialization and energy consumption, which led to the burning of fossil fuels (coal, oil, natural gases, etc.), principally responsible for climate change and global warming [1]. As a result, it causes the release of greenhouse gases, where carbon dioxide (CO₂) is the highest contributor with the annual average at Earth's surface at 409.8 ± 0.1 ppm globally (the year 2019), and it continues to grow [2]. As a result, there is an urgent need to reduce global CO₂ emissions. Three major existing methods have been demonstrated for CO₂ capture—oxy-fuel combustion, pre-combustion, and post-combustion [3]—from which the capture technology based on post-combustion has great potential for the reduction of CO₂ emissions, which uses various sorbents like zeolites, metal-organic frameworks (MOFs), covalent organic frameworks (COFs), and activated carbons (ACs) [4, 5]. Among these sorbents, AC materials have been widely used because of their low cost, stability, availability of large surface area, etc. [6, 7]. Therefore, there is growing interest among academic researchers and industry in reducing CO₂ emissions

where AC-based adsorption technologies have received greater attention.

Apart from the CO₂ emissions, water pollution is also one of the major environmental issues resulting from industrialization. Organic dyes are the significant source causing water pollution, especially azo dyes which belong to many industries, including textile, dyeing, printing, cosmetics, and pharmaceuticals [8]. These dyes have been characterized as hazardous and carcinogenic substances which can damage organs in human beings. Azo dyes are mainly classified as monoazo, diazo, triazo, polyazo, azoic, etc. From these azo dyes, monoazo dye (-N=N-) such as methyl orange (MO) is a widely used dye for the dyeing process, which is mutagenic, carcinogenic, and toxic to aquatic organisms. It is challenging to remove MO dye from wastewater by degradation, mainly due to chromophore and aromatic structure in the MO [9]. Even trace of this dye is causing harmful effects on human beings and aquatic life because of their stability and resistivity towards degradation. Therefore, the effluent containing these dyes must be removed to reduce their hazardous effect before discharging into the water. Numerous methods are used to remove azo dye waste from the water, such as photodegradation, coagulation, advanced oxidation, membrane separation, electrochemical, and biological methods [10]. However, these methods had some disadvantages: formation of by-products, high operating expenses, partial dye removal, high energy, etc. Therefore, traditional sorbents are now used to remove azo dyes due to their ease of operation, simplicity, huge availability, and efficiency.

Considering these severe environmental facts, many types of sorbents, including zeolites, porous silica, metal oxides, MOFs, COFs, and porous AC materials, have been developed and tested for both CO₂ capture and dye removal from wastewater [11, 12], where porous carbon-based materials are the most widely used sorbents [13]. In addition, these carbon-based materials are broadly classified into traditional carbon materials (carbon blacks and AC) and nanostructured carbons (CNTs, graphene, fullerenes). ACs are considered most important materials due to their tunability towards large specific surface area (SSA) and pore volume [14]. Further, the AC exhibits hierarchical porous structures with ordered micro-, meso-, and macropores, and their functional combination demonstrates surprisingly better sorbents for many industrial applications, including gas/vapor capture and water purification applications [15]. Specifically, the hierarchical porous ACs showed excellent sorption capacities towards CO₂ as well as different dyes [16, 17]. On the other hand, the hierarchical porous AC is an amorphous solid material that can be derived from various carbon-rich materials, including lignin, coal, charcoal, and agro-waste [18]. Out of these, the use of agro-waste can help to reduce the production cost and contribute to the recycling of waste to create an eco-friendly environment [19]. The hierarchical

porous ACs can be prepared by carbonizing agro-waste using pyrolysis or different carbonizing agents such as H₂SO₄ [20, 21], HNO₃ [22], and H₃PO₄ [21, 23]. However, the porosity and SSA enhancement have been extensively achieved by physical activation in N₂, CO₂, Ar, or chemical activation using KOH, ZnCl₂, etc., to obtain the desirable adsorption properties utilized for potential applications [18, 21, 24]. Sugarcane pith (SCP) is a fibrous agro-waste that is produced globally from the sugar production process. Globally, about 8 to 10 tonnes of SCP is produced per hour, while some of the SCP is reused mainly in paper manufacturing, most of the trash is burnt, leading to a further increase in CO₂ emissions [25].

The properties of AC are mainly depending on the route of preparation, carbon source, and especially on the activation path. By considering these aspects, we report a facile and economic template-free strategy to prepare hierarchical porous AC from SCP that can be used as a dual-purpose material to combat air and water pollution. The hierarchical porous AC produced by post nitrogen activation shows a high SSA and a significant capacity for CO₂ adsorption. Moreover, the highly porous material has a good adsorption capacity towards MO. The adsorption kinetics and thermodynamics of both CO₂ capture and MO adsorption are evaluated using different models, and the best parameters describing the adsorption process on AC are reported. This is the first demonstration of hierarchical porous AC produced from SCP for potential CO₂ capture and dye removal to the best of our knowledge. The enhanced sorption of CO₂ and MO show that SCP could be potentially used for environmental remediation instead of causing pollution upon burning.

2 Experimental

2.1 Materials and methods

Concentrated H₂SO₄ was purchased from Loba Chem Chemical Reagent Co. Ltd. The N₂ gas utilized for activation and CO₂ gas are purchased at a purity of > 99.9%. All chemical reagents were of analytical grade.

The agro-waste SCP obtained from the local area (Shirol Tahsil, Maharashtra, India) was washed with distilled deionized (DI) water and dried under sunlight for 3 days to use as a source for AC. The dried SCP was ground to powder and separated using the sieves to obtain ~25–50-micron particle size. Further, the SCP powder was subjected to acid carbonization as per the previous report [20]. Briefly, the SCP was soaked in concentrated H₂SO₄ with an impregnation ratio of 1:1 for 24 h. The mixture was stirred more frequently for complete carbonization of SCP. After the impregnation, the residual solid separated from the liquid washed with DI water for

removal of acid and dried at 373 K for 12 h under vacuum. Finally, the product residual carbon (RC) was thoroughly ground in a mortar to obtain a fine powder. The obtained RC was then subjected to temperature activation procedure in a tube furnace under N_2 flow at 773 K for 3 h with 10 K min^{-1} rate. This activation generally helps to introduce newer micropores with broadening of existing mesopores. The resulting RC and AC samples were stored in an inert atmosphere.

2.2 Characterization

The products RC and AC were characterized to determine their characteristic properties. The crystalline nature of RC and AC was determined using powder X-ray diffraction (PXRD) analysis on a Philips X-ray diffractometer employing nickel-filtered $Cu\ K\alpha$ radiation (scan rate: 1° min^{-1}) between 10 and 70° . The SSA and pore volume determinations were carried out from N_2 adsorption–desorption isotherms at a relative pressure (P/P_0) 0.99 and 77 K using a Brunauer–Emmett–Teller (BET) analyzer, Bellsorp mini II (Japan). The Barrett–Joyner–Halenda (BJH) method was employed to determine pore size distributions from adsorption branches of the isotherm. The field emission scanning electron microscope (FE-SEM) micrographs were obtained using JEOL JSM-6360. Prior to these measurements, the samples were degassed under a vacuum at 573 K for 5 h to remove the guest molecules from the sample. The Fourier transform infrared (FTIR) spectra were recorded in 400 – 4000 cm^{-1} on FTIR-4600, Jasco, Japan model. The elemental analysis (C, H, and N) was carried out using an elemental analyzer (Thermo, Finnigan), and the mass percentage of oxygen was determined by the subtraction method. The X-ray photoelectron spectroscopy (XPS) was performed using a Shimadzu ESCA 3400 instrument.

2.3 CO_2 adsorption isotherms

For CO_2 adsorption experiments, the samples RC and AC were degassed at 573 K for 5 h under a constant vacuum ($\sim 10^{-6}$ to 10^{-7} mbar) to remove the guest molecules from the pores. The CO_2 isotherms were recorded at 288, 298, and 308 K at 1 bar using a gas adsorption analyzer (Bellsorp mini II) using a static volumetric method to determine the CO_2 uptake capacity. The isosteric heat of adsorption (Q_{st}) of CO_2 is calculated for both the samples from these CO_2 adsorption isotherms. These adsorption isotherms were further studied for single-site and dual-site Langmuir models to determine the correlation of adsorption (ESI Eqs. 1 and 2). The CO_2/N_2 selectivity study for AC was carried out according to Henry's law (ESI Eqs. 3–5).

2.4 Dye removal studies

To examine the applicability of the AC for effluent treatment applications, a MO dye is used as a model organic pollutant. A stock solution of 500 ppm was prepared in DI water and used to prepare further concentrations for adsorption experiments. The adsorption studies were conducted using 0.1 g AC and 50 mL aqueous solution of MO dye of 10 to 300 ppm concentrations. The percentage dye removal (E%) (ESI Eq. 6) and adsorption kinetics was determined from the 10 ppm MO dye experiment, while adsorption capacity (q_t) and equilibrium adsorption capacity (q_e) of the AC for MO were determined using Eqs. 7 and 8 (ESI) respectively. The dye and AC were continuously mixed with shaking on an orbital shaker at 200 rpm to ensure complete mixing and to attain equilibrium. The 2 mL dye solution fractions were collected at 5- to 30-min time intervals and filtered through a $0.22\text{-}\mu\text{m}$ nylon syringe filter. The absorption spectra of resulting dye solutions were recorded on a UV–Vis spectrophotometer (UV-3000, Lab India).

3 Results and discussion

The illustration of agro-waste SCP converted into AC with wide micro- and mesopores having large SSA along with properties, which was responsible for enhancement for CO_2 and dye adsorption is given in Fig. 1. For the preparation of AC from RC, the simple strategy was followed with two steps: chemical carbonization and physical activation. Instead of thermal treatment for carbonization, we used chemical carbonization treatment where non-carbon species are removed from raw material which reduces cellulose, hemicellulose, and lignin crystallinity and that results in an increase in surface area for high CO_2 capture and environmental remediation.

3.1 Structural characteristics and chemical properties of carbons

The structure of the obtained RC and AC materials was studied by PXRD patterns shown in Fig. 2a. The RC material showed peak at around 19° results C (002) plane exhibits amorphization, whereas the AC reveals two diffraction peaks at 23° and 44° , corresponding to C (002) and C (101) planes of carbon [26].

The corresponding peak at 44° formed after the N_2 activation, which indicates the graphitization of carbon to some extent with a stacking-like structure. The existence of a broad peak C (002) between 15 and 30° could be attributed to amorphous carbon post-activation. The shift in broader

Fig. 1 Agro-waste SCP converted into hierarchically porous activated carbon with illustration of the content on the AC surface for CO₂ and dye adsorption

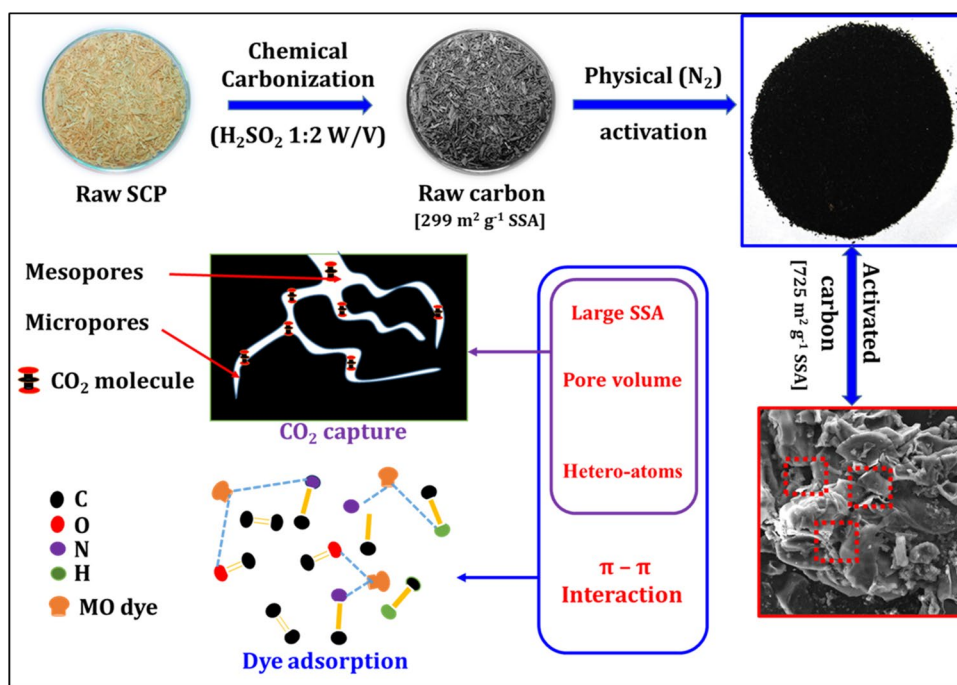
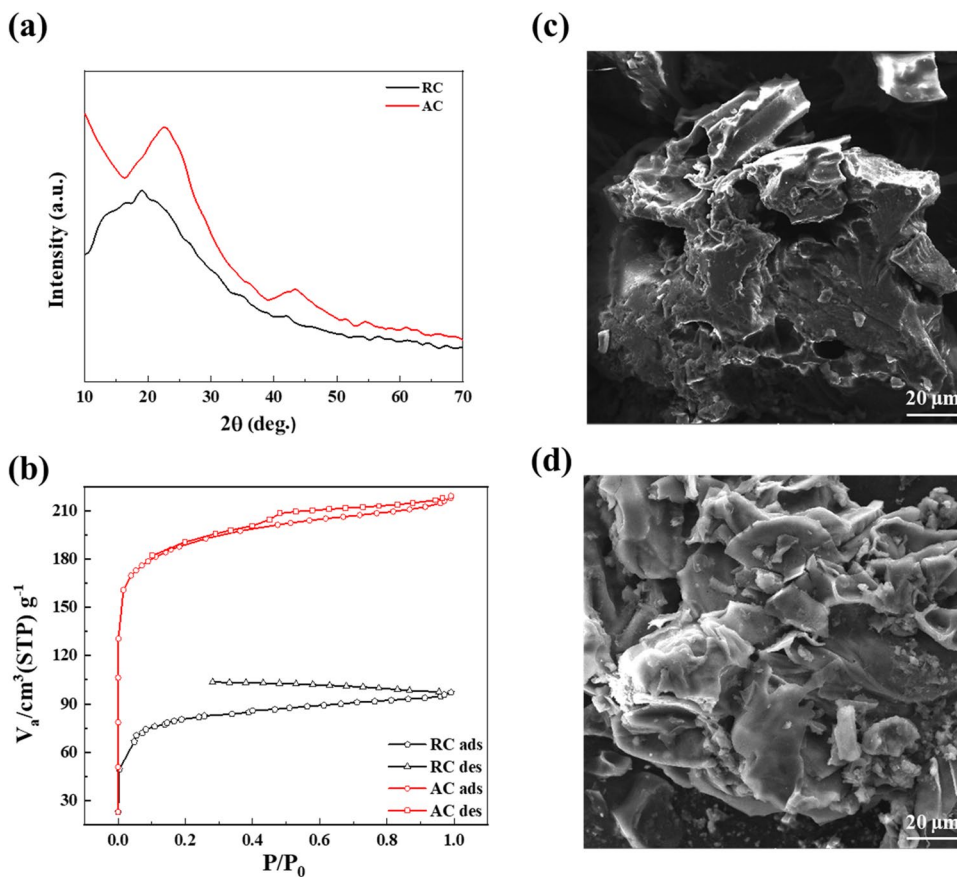


Fig. 2 (a) PXRD pattern, (b) BET adsorption–desorption profile, (c) FE-SEM micrographs of RC, and (d) FE-SEM micrographs of AC



peak position post-activation reveals changes in the d-spacing of material, which signifies increasing regularity of the structure [27].

To compare the porosity of RC and AC, N₂ adsorption–desorption isotherms and pore size distribution (PSD) were carried out using BET presented in Fig. 2b.

The obtained values of SSA (S_{BET}), Langmuir surface area (a_{sLang}), total pore volume (V_{total}), monolayer volume (V_{m}), ultra-micropore volume (V_{p}), and pore diameter (D_{p}) are as given in Table 1. The S_{BET} and V_{total} for RC are obtained to be $299.62 \text{ m}^2\text{g}^{-1}$ and $0.15 \text{ cm}^3\text{g}^{-1}$, respectively. After N_2 activation, SSA and total pore volume for AC are significantly increased to $725.91 \text{ m}^2\text{g}^{-1}$ and $0.34 \text{ cm}^3\text{g}^{-1}$, respectively, while Langmuir surface area for RC and AC is found to be $388.36 \text{ m}^2\text{g}^{-1}$ and $939.32 \text{ m}^2\text{g}^{-1}$, respectively. The N_2 adsorption/desorption isotherm curve indicates that the nitrogen activation can significantly increase the adsorbed volume due to the enhancement of surface area and pore volume of carbons by opening the pores through the removal of unreacted matter from it. Based on the IUPAC classification, the resulting N_2 adsorption/desorption isotherms for RC and AC carbons have exhibited a type IV curve with an H4 hysteresis nature but in case of RC hysteresis loop opened at low pressure range due to the structural changes in the AC leads to hysteresis in adsorption isotherm [28]. The textural information can be obtained by interpreting the resulting hysteresis loop for mesoporous materials. The PSD of RC and AC calculated from N_2 isotherms using non-local density functional theory (NLDFT) method indicates the existence of micropores in the carbons centered below 2 nm (Figure S1). The inset in Figure S1 shows that both RC and AC consist of micropores with a peak centered at 0.80 nm ($> 1 \text{ nm}$). The presence of such micropores is beneficial for the volume-filling mechanism; however, activation increases micropore volume which enhances the adsorption phenomenon drastically in AC.

The PSD also shows presence of mesopores centered at $\sim 29 \text{ nm}$. Through the nitrogen activation process, micropores are formed along with broadening mesopores, which results in a PSD centered at a smaller $\sim 12 \text{ nm}$ peak. The PSD of RC showed a similar mesoporous peak. Therefore, in RC and AC, the presence of micro- and mesopores was observed simultaneously. Although mesopores do not directly participate in CO_2 adsorption, they do provide easy

diffusion/accessibility to micropores within them which results in enhanced adsorption capacity of AC. The pre-treatment using H_2SO_4 in the production of RC is crucial to reduce non-carbon species from the internal structure and reduce the crystallinity of RC. The opening of pores was also confirmed from FE-SEM images (Fig. 2c and d). The surface morphology of the sampled AC changes a lot compared to RC, and it is composed of large pores with plentiful open cavities. The appearance of pores on AC surfaces is a result of the removal of volatiles and impurities during activation, effectively unblocking any clogged pores. The RC produced from H_2SO_4 was broken into irregular pores with smaller sizes and shapes, which means nitrogen activation significantly cracks up the RC structure and has the potential to promote an effective adjustment on the porosity of the resulting AC. Thus, it can be seen that the N_2 activation is significant to fabricate AC with high surface area and capable of increasing porosity, which can be explored in environmental remediation.

The CHN analysis of RC and AC shows the increase in C content from 55.9 to 71.9%, while the oxygen content decreases from 35.29 to 17.28% (Table 2). The XPS analysis also reveals the increase in nitrogen content which will be helpful to improve the CO_2 adsorption as well as environmental remediation. This proves that N_2 activation improves the purity as well as properties of AC. Additionally, it was observed that the hydrogen content in AC decreases slightly which may be due to the removal of volatile matter from RC; this observation was further confirmed from the FTIR results, and the remaining functional groups on RC and AC surfaces were analyzed using the FTIR analysis (Fig. 3). A broader band at 3427 cm^{-1} and 1398 cm^{-1} is attributed to the presence of -OH stretching vibration peak or N-H from amines and O-H bend, which is mainly due to the hydrogen bond in carboxylic, phenols, and alcohols from both carbons. The characteristic peak observed at 2923 cm^{-1} and 1029 cm^{-1} was caused by the -CH symmetric or asymmetric stretching vibration in the aliphatic hydrocarbons, and C-O

Table 1 Textural properties of RC and AC materials derived from SCP

Sample	S_{BET} (m^2/g)	A_{sLang} (m^2/g)	V_{total} (cm^3/g)	V_{m} (cm^3/g)	V_{p} (cm^3/g)	D_{p} (nm)
RC	299.6	388.36	0.1502	68.83	0.0440	2.004
AC	725.9	939.32	0.3377	166.78	0.0771	1.860

Table 2 Elemental composition from ultimate and XPS analysis of RC and AC materials derived from SCP

Sample	From ultimate analysis (%)				From XPS analysis (%)		
	C	H	N	O*	C	N	O
RC	55.9	8.16	0.60	35.29	71.4	0.7	28.0
AC	71.9	10.0	0.68	17.28	89.9	1.0	9.1

*Determined by difference

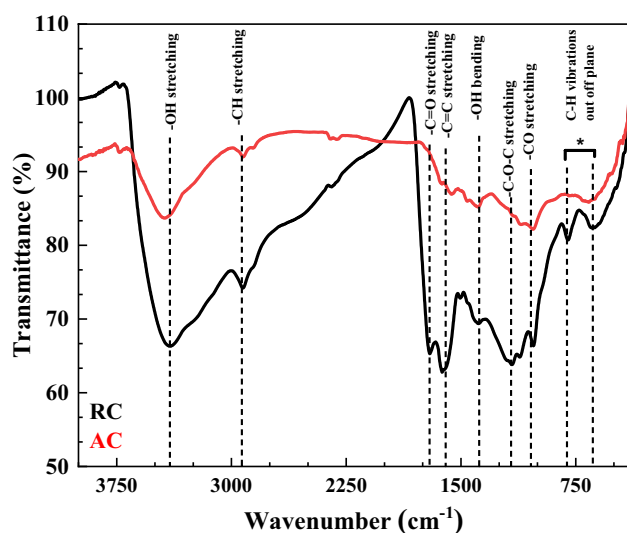


Fig. 3 FTIR spectra of RC (black) and AC (red) materials

bond stretching vibrations in organic compounds such as alcohols, phenols, acids, ethers, or esters, respectively [29, 30]. The peak at 795 cm^{-1} and 656 cm^{-1} is attributed to the cut-off plane bending vibrations of -CH bonds. The peak at 1711 cm^{-1} and 1620 cm^{-1} was assigned to the C=O stretching vibration of carboxyl or carbonyl groups and C=C stretching of conjugated alkenes [31]. After activation, the AC sample shows the same spectrum but the peak intensities of formed groups were decreased and slightly shifted to lower wavenumber; this was probably due to the possible molecular interactions. The characteristic peak at 1163 cm^{-1} is due to C–O stretching vibrations (e.g., in C–O–C glycosidic linkages of oligosaccharides or in triacylglycerols) only obtained in RC. It is noted that the relative intensities of the peak corresponding to the inner C–O group in AC disappear which shows graphitization of carbon with decrease in O content from C–O–C linkages, and this is also confirmed from CHN and XPS analyses (Table 2).

The XPS technique was performed to evaluate the elemental composition, functionalities, and oxidation states of both RC and AC (Fig. 4). The survey spectrum of both RC and AC shows high-intensity peaks corresponding to C and O. However, the spectrum shows the absence of peaks corresponding to sulfur and phosphorus while the trace amount of nitrogen is observed in both materials (Figure S2) and is in good agreement with the CHN results. The analyzed C 1 s and O 1 s spectra are deconvoluted and fitted using the Gaussian fitting method. The high-resolution C 1 s spectrum of RC and AC can attribute to corresponding binding energies of 284.7, 286.1, 288.0, and 292.13 eV which can be ascribed to the presence of C=C, C–O/C–N, O–C=O, and carbohydrate linkage groups respectively [32, 33]. The high resolution of the O 1 s spectrum of both AC

and RC materials can be fitted by four peaks, which reveals the appearance of peaks corresponding to C=O, O–H, C–O–C, and water clusters located at 531.3, 532.6, 533.1, and 535.1 eV, respectively [34]. Meanwhile, the contents of C, N, and O of both materials are summarized in Table 2. It is important to note that even an increase in a trace amount of N in AC could be contributed to the formation of pores which may be contributed to the enhancement of the adsorption phenomenon. It can be noted that the spectrum of RC material shows high-intensity peaks corresponding to the O with lower C intensity while the intensity corresponds to C increase with decreasing O intensity in AC; this attributes that the graphitization of carbon occurs which was supported from CHN and FTIR results.

3.2 CO₂ adsorption capacity

The CO₂ adsorption isotherms of RC and AC were recorded by the volumetric method [35], and CO₂ adsorption capacities were investigated at a temperature of 298 K shown in Fig. 5a and the resulting data are listed in Table 3. The comparison of all three temperatures is shown in Figure S3. The material AC possesses the highest CO₂ adsorption capacity of 2.71 mmol g^{-1} at 288 K (1 atm). This value is in good agreement with previously reported results derived from agro-waste for CO₂ capture. The RC exhibits CO₂ capacity (around 0.89 mmol g^{-1}) at 288 K and 1 atm, which is lower than that of the AC due to weak chemical interactions between the CO₂ and carbon surface. As expected, from Figure S3, it is observed that the amount of CO₂ adsorption decreases with a temperature rise in both samples at different adsorption temperatures. The material AC exhibits the CO₂ adsorption capacity of 2.72, 2.35, and 2.08 mmol g⁻¹ while for RC the adsorption capacity is 0.89, 0.73, and 0.61 mmol g⁻¹ at 288, 298, and 305 K and 1 atm, respectively. Higher CO₂ capture was observed at a lower temperature (288 K) which can be attributed to the exothermic nature of the CO₂ capture process (Figure S3). The activation process was found to be significant in enhancing the capture capacity as compared to their carbonized counterpart [36].

The CO₂ adsorption capacity was found to be higher in AC as compared to RC, reasoning, the AC has the highest SSA ($725\text{ m}^2\text{ g}^{-1}$), which is mainly due to the formation of a large number of micropores (<2 nm) as compared to RC (SSA $299.62\text{ m}^2\text{ g}^{-1}$). Also, the micropore volume for AC was found to be $0.3174\text{ cm}^3\text{ g}^{-1}$ which is about 3 times more than that of RC ($0.1402\text{ cm}^3\text{ g}^{-1}$). The volume of micropores below 2 nm has shown a good relationship with the CO₂ adsorption capacity (1 bar) which showed that the volume-filling mechanism for CO₂ adsorption established this size limit. The interaction energy between the CO₂ molecules and AC material is enhanced when the adsorption occurs in

Fig. 4 XPS spectra of RC and AC material, (a and b) survey; (c and d) C1s; (e and f) O1s spectra respectively

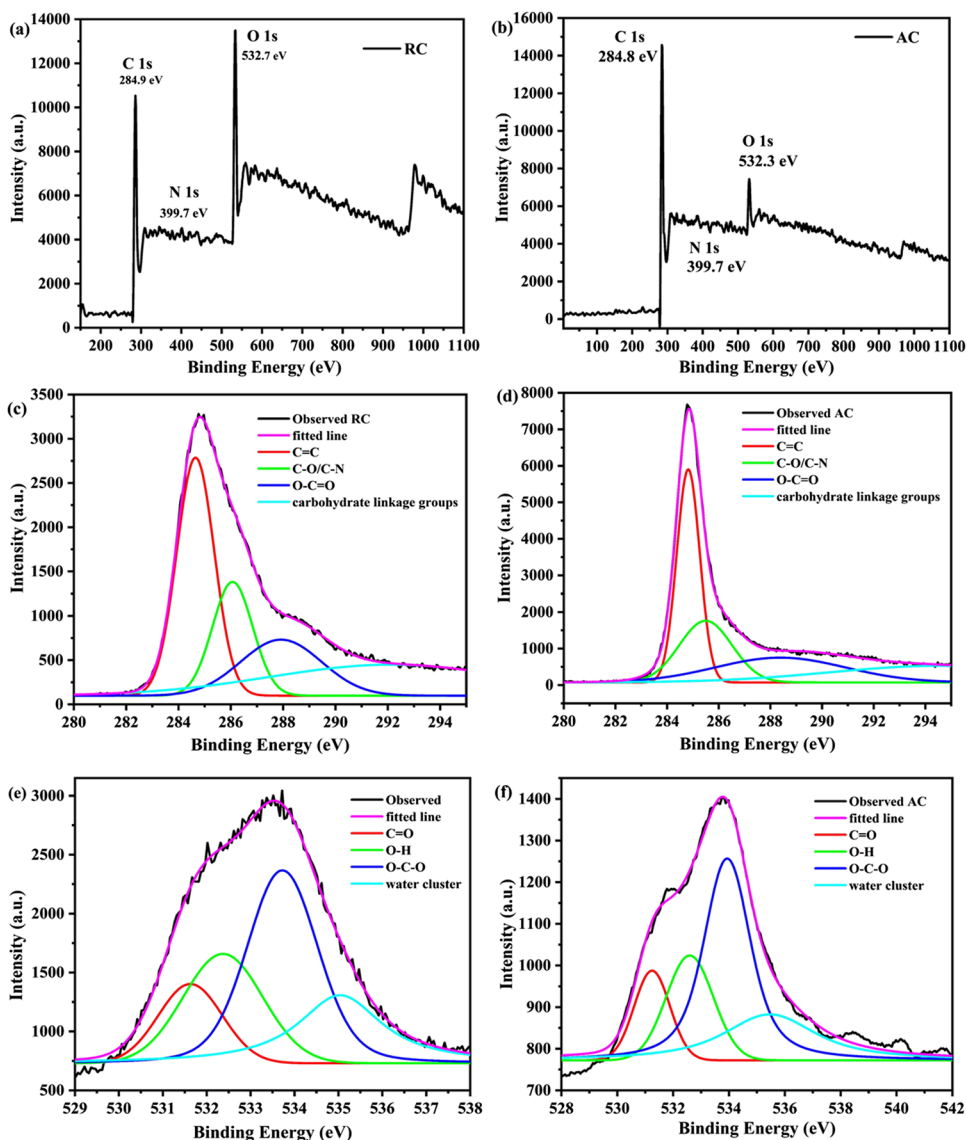
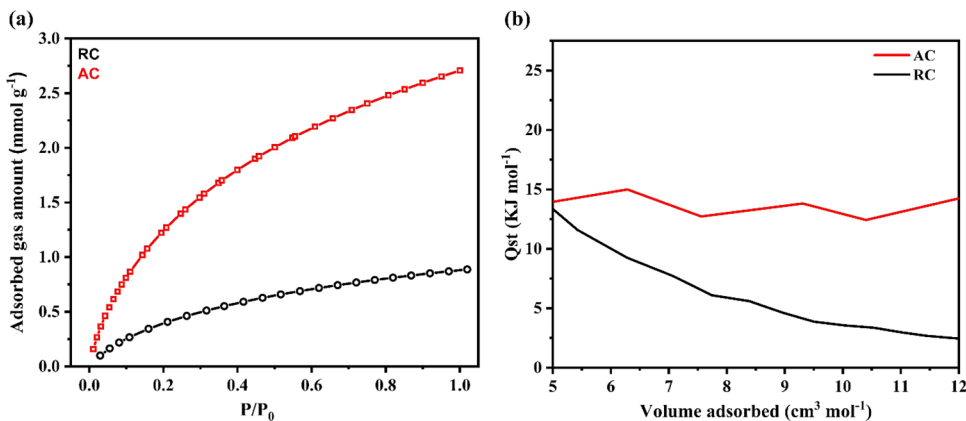


Fig. 5 CO₂ adsorption isotherms (a) of RC and AC materials at 298 K; (b) comparison of Q_{st} of RC and AC for the adsorption of CO₂ calculated using the dual-site Langmuir isotherm fits



micropores, ascribed that the overspread of potential fields from the neighboring walls. Furthermore, AC’s comparatively high nitrogen content (1%) contributes to higher CO₂

capacity than RC where its nitrogen content is 0.69%. The weak interaction between RC and CO₂ mainly occurred due to obstruction by the tar and impurities into the pores;

Table 3 CO₂ adsorption performance of RC and AC (at 1 atm P)

Sample	BET surface area (m ² /g)	Adsorption capacity (mmol/g)	T (K)
RC	299	0.89	288
		0.73	298
		0.61	308
AC	725	2.72	288
		2.35	298
		2.08	308

however, when RC is exposed with the physical activation under N₂ assists to increase the pore volume by removing such impurities resulting in the boost of CO₂ adsorption capacity. The CO₂ capacity has supposed as a keyword of the V_p analyzed with the help of BJH plot showed the improvement in the V_p (0.044 cm³g⁻¹) of RC to 0.077 cm³ g⁻¹ in AC inferred in to increment in SSA and total pore volume which enhances the CO₂ adsorption capacity. From practical aspects, it was observed that the N₂ activation is a constructive course of action to fabricate hierarchical porous structures in AC, which is closely associated with the SSA, pore volume, as well as nitrogen content, playing an important role in determining the CO₂ adsorption capacity [37].

The CO₂ capture amount for hierarchical porous AC is higher than that of other agro-waste-derived AC materials (Table S2). Compared to the other porous materials recently reported for CO₂ capture, the sample hierarchical porous AC demonstrates a comparable and good CO₂ capture capacity of 2.35 mmol g⁻¹ at 298 K and hence will be applicable as a favorable CO₂ adsorbent.

3.3 CO₂/N₂ selectivity

The adsorption selectivity nature of AC for CO₂ and N₂ was carried out at 288 and 298 K (shown in Figure S10) by measuring their adsorbed amounts at the same pressure. The maximum N₂ adsorption was found to be 0.43 mmol g⁻¹; however, this adsorption capacity for CO₂ has reached 2.72 mmol g⁻¹ at 288 K and 1 atm. Further, the CO₂ and N₂ adsorption isotherms were fitted with a simplified virial-type equation (ESI Eq. 3) and CO₂/N₂ selectivity calculated from Henry's law constant (Eq. 1) as follows [38, 39]:

$$S_{ij} = \frac{K_H(i)}{K_H(j)} \quad (1)$$

where $K_H(i)$ and $K_H(j)$ are Henry's constants for CO₂ and N₂, respectively (Table S1). The AC exhibits high adsorption selectivity of 21.41 and 19.87 for CO₂ over N₂ at 288 K and 298 K, respectively. Our results showed that the selectivity is remarkably higher as compared to the other agro-derived

carbons reported in the literature [40]. Therefore, AC obtained from SCP could be a promising and selective adsorbent for CO₂ and may be explored for the separation of CO₂ and N₂.

3.4 Isosteric heat of adsorption (Q_{st})

The Clausius–Clapeyron equation (Eq. 2) was employed to understand the surface interactions of AC and RC from the CO₂ adsorption isotherms at 288 and 298 K.

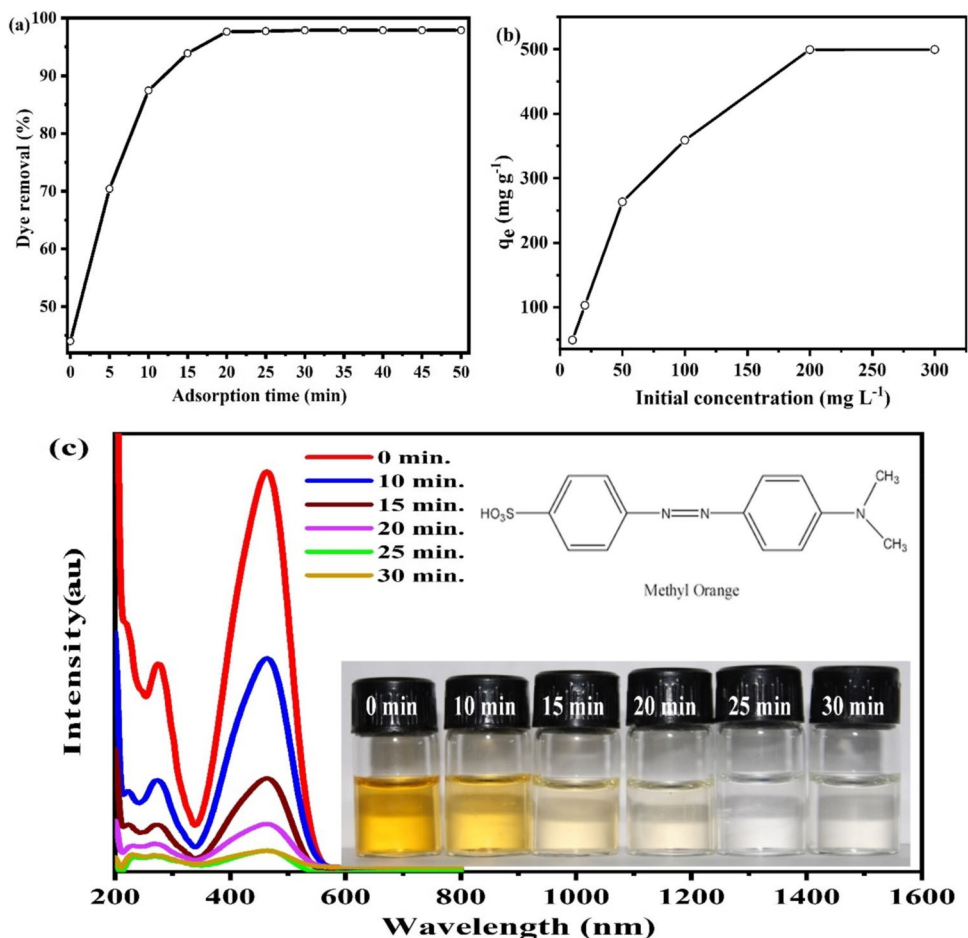
$$Q_{st} = RT^2 \left(\frac{\partial \ln P}{\partial T} \right) \quad (2)$$

We have noted that the Q_{st} value for the CO₂ adsorption in the RC and AC decreases with an increase in adsorption capacity. As illustrated in Fig. 5b, the Q_{st} for the AC is varied from 13.36 to 2.56 kJmol⁻¹, while for the RC it is in the range of 32.10 to 30.80 kJmol⁻¹. The Q_{st} values of RC and AC are below > 40 kJmol⁻¹ suggesting a physical adsorption nature of the material. Even the trends in the Q_{st} value for both samples are the same, the Q_{st} value in AC is lower than RC. This attributes that the micropores in the AC are fully occupied and then reach a saturation level with high amounts of CO₂ uptake (2.01 mmol g⁻¹) while in the case of RC all sites are occupied at a lower amount of CO₂ (0.61 mmol g⁻¹) which suggests relatively strong interactions between CO₂ molecules and pore walls of carbons [41, 42]. Therefore, low heat of adsorption of CO₂ is of clear interest as they will provide high selectivity. The Q_{st} decreases swiftly with an increase in adsorbed capacity for CO₂ affirming the heterogeneity in the adsorption. The fitting results obtained from different models are summarized in Figure S4, S5, S6, and S7, which shows that the adsorption behavior of CO₂ on AC is in accordance with the dual-site Langmuir model (R² = 0.9999), suggesting adsorption energy on the AC surface is uniform and remains unchanged [43, 44].

3.5 Methyl orange (MO) dye adsorption kinetics and equilibrium study

The adsorption kinetic study of MO was carried out to analyze the effect of time on the removal of MO (Fig. 6a). In this work, the efficiency of AC for the removal of MO from aqueous solutions was studied. The effects of dye removal experiments were performed using a dye solution of 10 ppm concentration. Figure 6c demonstrates that AC shows efficient and fast (within 25 min) adsorption of MO that may be due to the presence of large vacant sites with high SSA and large pore volume. The adsorption equilibrium obtained from the kinetic curve shows that AC achieves adsorption equilibrium within 20 min, resulting in the removal of 97.8% (± 0.5) of MO at room temperature. This may be attributed to the stronger electrostatic attraction forces between the dye

Fig. 6 (a) Adsorption rate of methyl orange dye on AC; (b) equilibrium adsorption capacity of AC for methyl orange dye, (c) UV–Visible spectra showing removal of dye w.r.t. time (inset in c shows photograph of dye removal w.r.t. time)



and AC as each molecule of MO has a negative charge. The equilibrium adsorption capacity (Fig. 6b) was determined using 10 to 300 ppm MO concentrations at 0 to 120-min time intervals. The study shows that the MO removal efficiency of AC decreases from 97.8 to 49.4% (± 0.5) reasoning unavailability of vacant sites on AC after initial adsorption which slows down the adsorption rate. It can be also attributed that after initial adsorption the repulsive forces between adsorbed dye and upcoming dye resulted in the decrease in adsorption capacity.

To understand dynamic adsorption characteristics and to determine the rate of adsorption of MO on the AC, linear forms of two kinetic models, pseudo-first-order (Eq. 3) and pseudo-second-order (Eq. 4), were used as below,

$$\ln (q_e - q_t) = \ln q_e - K_1 t \tag{3}$$

$$\frac{t}{q_e} = \frac{1}{K_1 q_e^2} + \frac{t}{q_e} \tag{4}$$

The adsorption data were fitted, and the parameters are listed in Table S3. The correlation coefficient (R^2) is determined for both kinetic models which (Figure S11) shows

a linear plot for MO adsorption on the AC for a pseudo-second-order kinetic model with good correlation coefficient ($R^2=0.99784$) than that of a pseudo-first-order kinetic model ($R^2=0.92543$). From the slope of the pseudo-second-order kinetic model curve, the theoretically calculated equilibrium adsorption (q_e , cal) of MO can be found in good agreement with the experimental adsorption capacity (q_e , exp). Therefore, the MO adsorption process is mainly controlled by the rate-limiting step [45, 46]. The maximum adsorption capacity of AC was obtained from adsorption equilibrium experiments using a series of different concentrations of MO solution. On the other hand, the concentration of dye solution (up to 300 ppm) increased the adsorption capacity, which is applied in equilibrium adsorption analysis for fitting different adsorption isotherm models such as Langmuir, Freundlich, and Temkin (ESI Eqs. 9–11) to determine the interaction between dye and adsorbents AC [47, 48]. The adsorption isotherm values calculated from these isotherm models are given in Table S4. Among three models, the Langmuir isotherm model showed a good correlation coefficient ($R^2=0.9850$) for adsorption of MO (Figure S12a). From the results, it is clear that Langmuir adsorption is a monolayer and homogeneous active site present on the solid

surface of the AC derived from sugarcane pith. As illustrated in Fig. 6b, the maximal MO adsorption capacity of the AC using the Langmuir isotherm model has been obtained to be 527.7 mg g^{-1} while experimental adsorption capacity is found to be 500.0 mg g^{-1} . This indicates that the AC is a good adsorbent for MO removal and able to achieve high adsorption capacity in a small time of equilibrium. The dye adsorption capacity of AC is comparable to other hierarchical porous structures derived from agro-waste and has been summarized in Table S5.

FTIR and XPS analyses suggest the presence of a significant number of acidic surface groups/some amount of aromaticity/hydrogen bonds on the surface of AC. This may be attributed to the stronger electrostatic attraction force among the SCP-AC and MO in the form of π - π , cation- π , and anion- π interactions due to the presence of hetero-atoms on its structure, negative charge on each MO molecule, and stronger chemical interactions that can account for a significant MO adsorption [46]. Also AC has large SSA and good porosity which ensures the higher accessibility of active surface/sites for MO adsorption (Fig. 1).

3.6 Regeneration and recycling of activated carbon for MO adsorption

Instead of solvent treatment, thermal treatment at 773 K for 60 min was employed to reproduce AC after adsorption of dye to minimize secondary pollution. The reusability of AC (Fig. 7a) shows that MO adsorption efficiency (E) for the second cycle decreased slightly and was observed to be 93.30%. However, the study shows a decrease in E to 87.08% for the subsequent 3rd cycle indicating the appreciable reusability of AC. The reduction in E may attribute to the blockage of pores due to MO molecules or its pyrolyzed products. Further, the activation of AC was confirmed from the FTIR study (Fig. 7b) which shows that the peaks similar to AC were observed in regenerated AC (ACR) as well as the absence of peaks corresponds to 1600 cm^{-1} and 1516 cm^{-1} for $-\text{N}=\text{N}-$ stretching vibrations and the peak at 1111 cm^{-1}

corresponding to $-\text{S}=\text{O}$ stretching vibrations confirms its regeneration from MO adsorbed AC (ACMO).

4 Conclusion

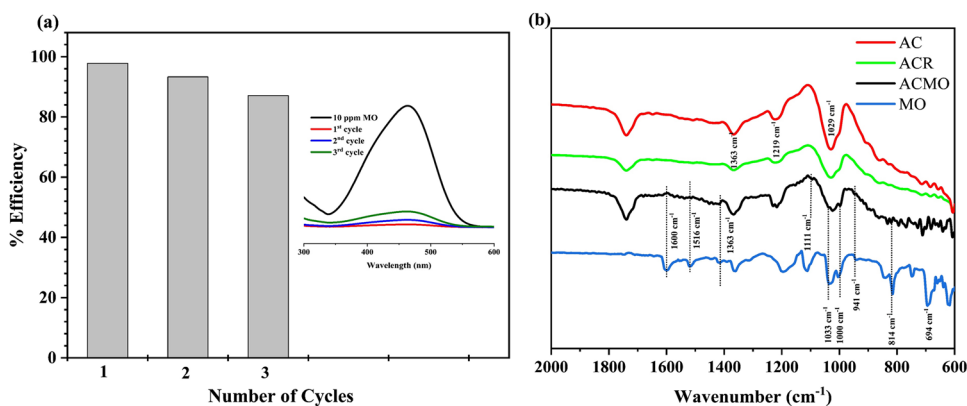
In summary, the abundantly available agro-waste sugarcane pith was successfully converted into ordered hierarchical porous activated carbon (AC) as an efficient adsorbent for CO_2 and methyl orange dye. Particularly, AC material possesses high SSA ($725.91 \text{ m}^2 \text{ g}^{-1}$) and total pore volume ($0.3377 \text{ cm}^3 \text{ g}^{-1}$), exhibits a high CO_2 adsorption capacity of 2.72 mmol g^{-1} at 273 K (1 atm). The material exhibits the simultaneous presence of micro- and mesopores with plenteous open cavities. The AC exhibits good selectivity for CO_2/N_2 and low isosteric heat of adsorption (Q_{st}) of 21.41 and $13.36 \text{ kJ mol}^{-1}$, respectively, and is the best fit with the dual-site Langmuir model. Further, AC showed a high equilibrium capacity (527.7 mg g^{-1}) and a faster removal rate of MO dye with pseudo-second-order kinetics. Considering the merits, the SCP was found to be the low cost and easily available source for AC which would be the promising material for CO_2 capture, storage, as well as the removal of dyes from wastewater. In addition, our results may serve as a guide for future studies for sustainable and clean energy-related applications.

Supplementary Information The online version contains supplementary material available at <https://doi.org/10.1007/s13399-022-03067-y>.

Acknowledgements A.K. and S.S. are thankful to the Department of Science and Technology, New Delhi, for the grant under the DST-FIST program (No/SR/FST/College-151/2013(C)) Jaysingpur College, Jaysingpur. A.K.B. and R.K.M. acknowledge the Laboratory Directed Research and Development (LDRD) program at the Pacific Northwest National Laboratory (PNNL). PNNL is operated by Battelle for the US Department of Energy (DOE) under Contract DE-AC05-76RL01830.

Author contribution Miss Amruta Koli: experimental work and writing original draft. Dr. Anil K. Battu: formal analysis and drafting support. Dr. Radha Kishan Motkuri: formal analysis, reviewing, and drafting

Fig. 7 (a) Regeneration study of AC under identical experimental conditions (AC = 100 mg; MO = 10 ppm) [inset UV-Vis. Spectra of remained dye after adsorption at different cycles]; (b) FTIR analysis of dye (MO), AC with adsorbed dye (ACMO), regenerated AC (ACR), and AC



support. Dr. Sandip Sabale: conceptualization, reviewing and editing, supervision, and laboratory support.

Declarations

Competing interests The authors declare no competing interests.

References

- Azorin-Molina C, Dunn R, Ricciardulli L et al (2020) Land and ocean surface winds [in “State of the climate in 2019”]. *Bull Am Meteorol Soc* 101:S63–S65. <https://doi.org/10.1175/2020BAMSStateoftheClimate.1>
- REBECCA LINDSEY Climate change: atmospheric carbon dioxide | NOAA Climate.gov. <https://www.climate.gov/news-features/understanding-climate/climate-change-atmospheric-carbon-dioxide>. Accessed 3 Sep 2021
- Matito-Martos I, Sepúlveda C, Gómez C et al (2021) Potential of CO₂ capture from flue gases by physicochemical and biological methods: a comparative study. *Chem Eng J* 417:128020. <https://doi.org/10.1016/j.cej.2020.128020>
- Bower JK, Barpaga D, Prodingler S et al (2018) Dynamic adsorption of CO₂/N₂ on cation-exchanged chabazite SSZ-13: a breakthrough analysis. *ACS Appl Mater Interfaces* 10:14287–14291. <https://doi.org/10.1021/acsami.8b03848>
- Thallapally PK, Tian J, Radha Kishan M et al (2008) Flexible (breathing) interpenetrated metal-organic frameworks for CO₂ separation applications. *J Am Chem Soc* 130:16842
- Wang J, Pu Q, Ning P, Lu S (2021) Activated carbon-based composites for capturing CO₂: a review. *Greenh Gases Sci Technol* 11:377–393. <https://doi.org/10.1002/ghg.2051>
- Mumtaz H, Farhan M, Amjad M et al (2021) Biomass waste utilization for adsorbent preparation in CO₂ capture and sustainable environment applications. *Sustain Energy Technol Assess* 46:101288. <https://doi.org/10.1016/j.seta.2021.101288>
- Zhao H, Wang J, Fan Z et al (2022) A facial synthesis of nitrogen-doped reduced graphene oxide quantum dot and its application in aqueous organics degradation. *Green Energy Environ* 7:440–448. <https://doi.org/10.1016/j.gee.2020.10.008>
- Iwuozor KO, Ighalo JO, Emenike EC et al (2021) Adsorption of methyl orange: a review on adsorbent performance. *Curr Res Green Sustain Chem* 4:100179. <https://doi.org/10.1016/j.crgsc.2021.100179>
- Benkhaya S, M’rabet S, El Harfi A (2020) Classifications, properties, recent synthesis and applications of azo dyes. *Heliyon* 6:e03271. <https://doi.org/10.1016/j.heliyon.2020.e03271>
- Liu J, Zheng J, Barpaga D et al (2018) A tunable bimetallic MOF-74 for adsorption chiller applications. *Eur J Inorg Chem* 2018:885–889. <https://doi.org/10.1002/ejic.201800042>
- Lan D, Zhu H, Zhang J et al (2022) Adsorptive removal of organic dyes via porous materials for wastewater treatment in recent decades: a review on species, mechanisms and perspectives. *Chemosphere* 293:133464. <https://doi.org/10.1016/j.chemosphere.2021.133464>
- Singh G, Lee J, Karakoti A et al (2020) Emerging trends in porous materials for CO₂ capture and conversion. *Chem Soc Rev* 49:4360–4404. <https://doi.org/10.1039/DOCS00075B>
- Serafin J, Kielbasa K, Michalkiewicz B (2022) The new tailored nanoporous carbons from the common polypody (*Polypodium vulgare*): the role of textural properties for enhanced CO₂ adsorption. *Chem Eng J* 429:131751. <https://doi.org/10.1016/j.cej.2021.131751>
- Acevedo S, Giraldo L, Moreno-Piraján JC (2020) Adsorption of CO₂ on activated carbons prepared by chemical activation with cupric nitrate. *ACS Omega* 5:10423–10432
- Estevez L, Barpaga D, Zheng J et al (2018) Hierarchically porous carbon materials for CO₂ capture: the role of pore structure. *Ind Eng Chem Res* 57:1262–1268. <https://doi.org/10.1021/acs.iecr.7b03879>
- Li J, Tian L, Liang F et al (2019) Molten salt synthesis of hierarchical porous N-doped carbon submicrospheres for multifunctional applications: high performance supercapacitor, dye removal and CO₂ capture. *Carbon* 141:739–747. <https://doi.org/10.1016/j.carbon.2018.09.061>
- Serafin J, Ouzzine M, Cruz Junior OF, Sreńscek-Nazzal J (2021) Preparation of low-cost activated carbons from amazonian nutshells for CO₂ storage. *Biomass Bioenergy* 144:105925. <https://doi.org/10.1016/j.biombioe.2020.105925>
- Paul S, Dutta A (2018) Challenges and opportunities of lignocellulosic biomass for anaerobic digestion. *Resour Conserv Recycl* 130:164–174. <https://doi.org/10.1016/j.resconrec.2017.12.005>
- Khan T, Isa MH, Mustafa MRU et al (2016) Cr (VI) adsorption from aqueous solution by an agricultural waste based carbon. *RSC Adv* 6:56365–56374
- Zhou X-L, Zhang H, Shao L-M et al (2021) Preparation and application of hierarchical porous carbon materials from waste and biomass: a review. *Waste Biomass Valori* 12:1699–1724. <https://doi.org/10.1007/s12649-020-01109-y>
- Noh JS, Schwarz JA (1990) Effect of HNO₃ treatment on the surface acidity of activated carbons. *Carbon* 28:675–682. [https://doi.org/10.1016/0008-6223\(90\)90069-B](https://doi.org/10.1016/0008-6223(90)90069-B)
- Kwiatkowski M, Serafin J, Booth AM, Michalkiewicz B (2021) Computer analysis of the effect of activation temperature on the microporous structure development of activated carbon derived from common polypody. *Materials* 14:. <https://doi.org/10.3390/ma14112951>
- Al Bahri M, Calvo L, Gilarranz M, Rodriguez J (2016) Diuron multilayer adsorption on activated carbon from CO₂ activation of grape seeds. *Chem Eng Commun* 203:103–113. <https://doi.org/10.1080/00986445.2014.934447>
- Powar RV, Mehrete SA, Powar TR, Patil SB (2022) End-use applications of sugarcane trash: a comprehensive review. *Sugar Tech*. <https://doi.org/10.1007/s12355-022-01107-5>
- Rahman HA, Chin SX (2019) Physical and chemical properties of the rice straw activated carbon produced from carbonization and KOH activation processes. *Sains Malays* 48:385–391. <https://doi.org/10.17576/jsm-2019-4802-16>
- Zhao J, Yang L, Li F et al (2009) Structural evolution in the graphitization process of activated carbon by high-pressure sintering. *Carbon* 47:744–751. <https://doi.org/10.1016/j.carbon.2008.11.006>
- Gao J, Xie J, Liu X, Hu H (2017) Preparation and evaluation of modified cyanobacteria-derived activated carbon for H₂ adsorption. *RSC Adv* 7:20412–20421. <https://doi.org/10.1039/C6RA28660G>
- Rouzitab Z, Maklavany DM, Rashidi A, Jafarinejad S (2018) Synthesis of N-doped nanoporous carbon from walnut shell for enhancing CO₂ adsorption capacity and separation. *J Environ Chem Eng* 6:6653–6663. <https://doi.org/10.1016/j.jece.2018.10.035>
- Coates J (2000) Interpretation of infrared spectra, a practical approach
- Nikonenko N, Buslov D, Sushko N, Zhbakov R (2000) Investigation of stretching vibrations of glycosidic linkages in disaccharides and polysaccharides with use of IR spectra deconvolution. *Biopolymers* 57:257–262. [https://doi.org/10.1002/1097-0282\(2000\)57](https://doi.org/10.1002/1097-0282(2000)57)
- Oswald S, Thoss F, Zier M et al (2018) Binding energy referencing for XPS in alkali metal-based battery materials research

- (II): application to complex composite electrodes. *Batteries* 4:36. <https://doi.org/10.3390/batteries4030036>
33. Wu C, Yang S, Cai J et al (2016) Activated microporous carbon derived from almond shells for high energy density asymmetric supercapacitors. *ACS Appl Mater Interfaces* 8:15288–15296. <https://doi.org/10.1021/acsami.6b02942>
 34. Sodtipinta J, Amornsakchai T, Pakawatpanurut P (2017) Nanoporous carbon derived from agro-waste pineapple leaves for supercapacitor electrode. *Adv Nat Sci Nanosci Nanotechnol* 8:035017. <https://doi.org/10.1088/2043-6254/aa7233>
 35. Burrell J, Bethea D, Troub B (2017) Combination volumetric and gravimetric sorption instrument for high accuracy measurements of methane adsorption. *Rev Sci Instrum* 88:053902. <https://doi.org/10.1063/1.4982889>
 36. Sevilla M, Fuertes AB (2011) Sustainable porous carbons with a superior performance for CO₂ capture. *Energy Environ Sci* 4:1765–1771. <https://doi.org/10.1039/C0EE00784F>
 37. Wang X, Xiong L, Li L, Zhong J (2020) Effect of heat treatment temperature on CO₂ capture of nitrogen-enriched porous carbon fibers. *Greenh Gases Sci Technol* 10:461–471. <https://doi.org/10.1002/ghg.1904?sid=researcher>
 38. Wang X-F, Xiong L, Zhong J-J et al (2020) Nitrogen-containing porous carbon fibers prepared from polyimide fibers for CO₂ capture. *Ind Eng Chem Res* 59:18106–18114. <https://doi.org/10.1021/acs.iecr.0c03318>
 39. Li K, Tian S, Jiang J et al (2016) Pine cone shell-based activated carbon used for CO₂ adsorption. *J Mater Chem A* 4:5223–5234. <https://doi.org/10.1039/C5TA09908K>
 40. Balou S, Babak SE, Priye A (2020) Synergistic effect of nitrogen doping and ultra-microporosity on the performance of biomass and microalgae-derived activated carbons for CO₂ capture. *ACS Appl Mater Interfaces* 12:42711–42722. <https://doi.org/10.1021/acsami.0c10218>
 41. Park HJ, Suh MP (2013) Enhanced isosteric heat, selectivity, and uptake capacity of CO₂ adsorption in a metal-organic framework by impregnated metal ions. *Chem Sci* 4:685–690. <https://doi.org/10.1039/C2SC21253F>
 42. González-Camuñas N Unusually low heat of adsorption of CO₂ on AlPO and SAPO molecular sieves. <https://doi.org/10.3389/fchem.2020.588712>
 43. Wang J, Guo X (2020) Adsorption isotherm models: classification, physical meaning, application and solving method. *Chemosphere* 258:127279. <https://doi.org/10.1016/j.chemosphere.2020.127279>
 44. Wang J, Wei Y, Ma Z (2020) Modified dual-site Langmuir adsorption equilibrium models from a GCMC molecular simulation. *Appl Sci* 10:1311. <https://doi.org/10.3390/app10041311>
 45. Zambare R, Song X, Bhuvana S et al (2017) Ultrafast dye removal using ionic liquid–graphene oxide sponge. *ACS Sustain Chem Eng* 5:6026–6035. <https://doi.org/10.1021/acssuschemeng.7b00867>
 46. Jia Y, Ding L, Ren P et al (2020) Performances and mechanism of methyl orange and congo red adsorbed on the magnetic ion-exchange resin. *J Chem Eng Data* 65:725–736. <https://doi.org/10.1021/acs.jced.9b00951>
 47. Qu W, He D, Huang H et al (2020) Characterization of amino-crosslinked hypromellose and its adsorption characteristics for methyl orange from water. *J Mater Sci* 55:7268–7282. <https://doi.org/10.1007/s10853-020-04517-6>
 48. Aljeboree AM, Alshirifi AN, Alkaim AF (2017) Kinetics and equilibrium study for the adsorption of textile dyes on coconut shell activated carbon. *Arab J Chem* 10:S3381–S3393. <https://doi.org/10.1016/j.arabjc.2014.01.020>

Publisher's note Springer Nature remains neutral with regard to jurisdictional claims in published maps and institutional affiliations.